

Article

Correlation between Cellular Structure Morphology and Anisotropic Yield in Additively Manufactured Stainless Steel 316L

Dae Woong Kim ¹, Soo Bin Han ², Yoon Sun Lee ², Dong Yong Park ², Ho-Jin Lee ² , Sung Hyuk Park ³ and Hyejin Song ^{2,*}

¹ Analysis & Assessment Group, Research Institute of Industrial Science & Technology, Pohang 37673, Republic of Korea

² Smart Manufacturing Technology R&D Group, Korea Institute of Industrial Technology, Daegu 72994, Republic of Korea

³ School of Materials Science and Engineering, Kyungpook National University, Daegu 41566, Republic of Korea

* Correspondence: shyjein@kitech.re.kr

Abstract: Additively manufactured austenitic stainless steel 316L is composed of a cellular structure, which has a directionality, and is observed with a different morphology depending on the observation direction. The cellular structure morphology that appears with a high probability in grains with a specific grain orientation is determined. Taylor factor, which is calculated by considering grain orientation, is related to cellular structure morphology due to the directional cellular structure in additively manufactured austenitic stainless steel 316L. The Taylor factor affects the mechanical properties. The yield strength of additively manufactured SUS316L can be explained by the correlation between cellular structure morphology, grain orientation, and Taylor factor.

Keywords: additive manufacturing; stainless steel; cellular structure; Taylor factor; Anisotropy



Citation: Kim, D.W.; Han, S.B.; Lee, Y.S.; Park, D.Y.; Lee, H.-J.; Park, S.H.; Song, H. Correlation between Cellular Structure Morphology and Anisotropic Yield in Additively Manufactured Stainless Steel 316L. *Materials* **2023**, *16*, 1666. <https://doi.org/10.3390/ma16041666>

Received: 3 January 2023

Revised: 6 February 2023

Accepted: 15 February 2023

Published: 16 February 2023



Copyright: © 2023 by the authors. Licensee MDPI, Basel, Switzerland. This article is an open access article distributed under the terms and conditions of the Creative Commons Attribution (CC BY) license (<https://creativecommons.org/licenses/by/4.0/>).

1. Introduction

Additive manufacturing (AM) can form complex shapes that are difficult to make with conventional processes such as rolling, forging, and casting. In addition, in line with the next-generation manufacturing trend of mass customization and flexible production, it has attracted attention as a new manufacturing technology in various industries such as automobiles, aerospace, chemicals, and marine [1–5]. Additively manufactured products experience complicated thermal cycles because of the process in which metal powder is repeatedly melted and solidified by a high-power laser or electron beam [2,6–8]. The continuous deposition in the AM process, results in a complex solidification microstructure, which can overcome the strength-ductility trade-off observed in conventional metal materials, while exhibiting excellent mechanical properties [1,9,10].

AM methods can be broadly classified into powder bed fusion (PBF) and direct energy deposition (DED). In particular, the DED method forms a melt pool by irradiating a high-power laser beam on the metal surface and simultaneously supplying metal power [7,11]. Because it is similar to the conventional welding method, it can be implemented on the surface of existing products, and can therefore be used for repair work. In addition, it is possible to manufacture alloys in real time using several types of powders simultaneously [4,11,12]. As mentioned above, the metal material manufactured by the AM method exhibits a complex solidification microstructure, as rapid melting and cooling repeatedly occur [13–15]. In particular, in the case of austenitic stainless steel, alloying elements are segregated along the cell boundaries in a face-centered cubic (FCC) matrix, and is known to have a sub-micro cellular structure decorated with alloying elements and tangled dislocations [2,10,16,17].

This cellular structure is related to the excellent combination of strength and ductility of the materials manufactured using AM. Cellular structure boundaries decorated with alloying elements and tangled dislocations contribute to the improvement of strength in the Hall–Petch relationship by interfering with the dislocation movement [2,10,18]. In addition, the cellular structure boundary can act as a dislocation nucleation site, so that the cell size can influence the strain hardening of the material [16]. Although there are many previous studies on the effect of cellular structure on mechanical properties, few studies focusing on the effect of the cellular structure morphology on the mechanical properties have been conducted.

Cell structure grows along the preferred growth direction, especially in crystals with FCC structure, the preferred growth direction is the $\langle 001 \rangle$ direction [2,19]. The cellular structure morphology depends on the observation direction of cellular structure grown in the grain, and research on the relationship between orientation of grain and cellular structure morphology is insufficient. In addition, growth direction of cell structure is affected by crystallographic texture, and research on the correlation between cell structure and texture is needed.

In this study, the correlation between cellular structure morphology, grain orientation, and the Taylor factor was analyzed through the microstructure analysis of the planes perpendicular to the building direction (BD) and transverse direction (TD) in SUS316L fabricated using the DED method. The effect of microstructure, particularly cellular structure, grain orientation, and Taylor factor on the yield strength was also analyzed. The difference in mechanical properties according to cell structure morphology was correlated through hardness and the Taylor factor. The difference in compression properties of the BD and TD directions was analyzed through the volume fraction analysis of each cellular structure morphology.

2. Materials and Methods

Austenitic stainless steel 316L powder was commercially produced and the average size of the powder was 110 μm . The chemical composition (Fe-18.4Cr-12.2Ni-3.07Mo-0.02C (wt.%)) of the powder was measured by X-ray fluorescence (XRF, SU8020, Hitachi). The specimen was additively manufactured with a rectangular parallelepiped (dimensions: 20 \times 20 \times 20 mm) using a DED machine (model: MX-3, InssTek), with fixed parameters of a laser power of 400 W, scan speed of 0.85 m/min, powder feed rate of 3 g/min, hatching space of 0.5 mm, and layer thickness of 0.25 mm. The scan strategy is depicted in Figure 1, which represents a cross-snake hatching method that rotates the hatching direction by 90° after stacking each layer.

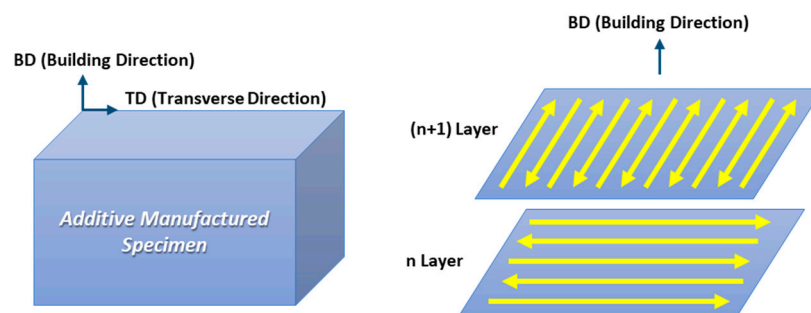


Figure 1. Schematic illustration showing the direction of the observation plane and scanning strategy in the additively manufactured specimen.

As depicted in Figure 1, the microstructures were analyzed in planes perpendicular to the transverse direction (TD) and building direction (BD), respectively. Additively manufactured stainless steel specimens were polished and etched in a solution of glycerol (45 mL), hydrochloric acid (30 mL), and nitric acid (30 mL), and the microstructures on the BD and TD planes of the specimens were observed using optical microscopy (OM) and field-

emission scanning electron microscopy (FE-SEM, model: JSM-7900F, JEOL). The orientation analysis and the Taylor factor of the specimens were analyzed using electron back-scatter diffraction (EBSD) analysis (OIM Data Collection 5 software, step size; $0.8\ \mu\text{m}$). Specimens for EBSD were prepared by mechanical polishing using a $0.04\ \mu\text{m}$ colloidal solution.

Cylindrical type specimens (diameter: 5π , height: 10 mm) were compressed parallel to transverse direction and building direction, respectively, using a universal testing machine (model: 5988, INSTRON) at room temperature with a strain rate of $10^{-3}\ \text{s}^{-1}$. All compression tests were performed three times to increase the reliability of the data. Vickers hardness tests for each cellular structure conducted 10 times at a constant load of 0.05 kgf (model: VH300, BUEHLER).

3. Results and Discussion

The melt pool boundaries are clearly visible in the low-magnification OM images of the BD and TD planes (Figure 2a,b), and the SEM images depict how the morphology of the cellular structure differs based on the melt pool boundaries (Figure 2c,d). During AM, a complex microstructure is formed owing to rapid and repeated thermal cycles [13–15]. Cellular structures are formed through epitaxial growth along the preferred crystallographic orientation, which is close to the temperature gradient (G) direction from the molten pool boundaries. According to the solidification theory, the preferred crystallographic orientation is $\langle 001 \rangle$ in alloys with FCC crystals such as austenitic stainless steel 316L [2,19]. As shown in Figure 3, the cellular structures may have different morphologies depending on the direction of observation, due to epitaxial growth [2]. When the cell growth direction is parallel to the observation direction, equiaxed type appears, as depicted in Figure 3b. When the cell growth direction and the observation direction are close to 45 degrees, an elongated cell structure, which is intermediate between equiaxed and lath-like types, is observed (Figure 3c). When the cell growth direction and observation direction are vertical, a lath-like type is observed, as depicted in Figure 3d.

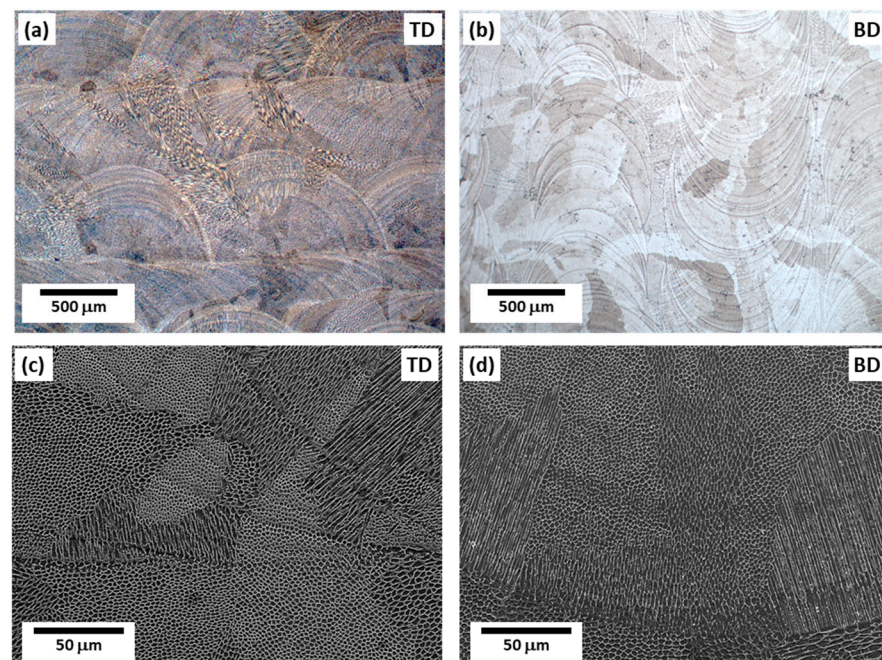


Figure 2. Microstructures of the specimen: (a,b) OM and (c,d) SEM images of the TD and BD planes, showing melt pool boundaries and cellular structures.

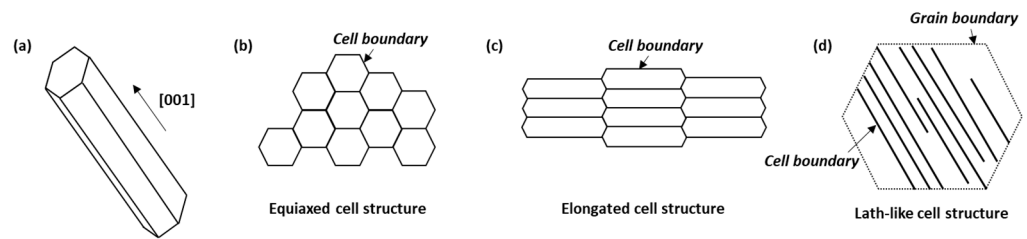


Figure 3. Schematic illustrations of (a) cell growth direction and (b–d) cellular structure types according to morphology.

Orientation analysis of the cellular structure morphology was performed based on the data obtained from EBSD (Figure 4). Figure 4a,b depicts the SEM backscattered electron (BSE) image in the same region as the EBSD inverse pole figure (IPF) image, corresponding to the TD plane of the specimen. Along the cellular structure boundaries, solute atoms are segregated during the solidification process due to the difference in solubility between solid and liquid, and a difference in contrast appears in the BSE image, which makes it possible to distinguish the cellular structure boundaries, thereby revealing the cellular structure morphology [2]. In Figure 4a,b, the grain composed of the cellular structure observed to be of lath-like type is grain 1; the grain observed as elongated type is grain 2; and the grain that appears as both elongated and lath-like cellular types is grain 3. The $\langle 001 \rangle$ plane traces of each grain are shown in the BSE image (Figure 4b). Here, grain 1 is identified as a grain composed of a typical lath-like cellular structure in which a parallel lath appears. Consequently, the lath direction is observed to coincide with one of the cell growth directions by comparing it with the red plane trace in the grain. Grain 2 is identified as cellular structure with an elongated shape, and the elongated direction coincides with the $\langle 001 \rangle$ direction. In the case of grain 3, elongated and lath-like types appear simultaneously. Because the growth of on grain is possible in each of the $[001]$, $[010]$, and $[100]$ directions, up to three types of cellular structure morphologies can be observed. Therefore, two types of cellular structures can be observed simultaneously in grain 3, where the elongated directions are also well matched with $\langle 001 \rangle$ (Figure 4b), which is the direction of cell growth.

Because cellular structures grow along the $\langle 001 \rangle$ direction, the probability of determining each type of cellular structure varies depending on the grain orientation. The equiaxed type is more likely to be observed closer to the $\langle 001 \rangle$ oriented grain on the IPF, which coincides with the cell growth direction. There are three $\langle 001 \rangle$ directions, and in the $\langle 001 \rangle$ oriented grain, the probability of finding the equiaxed and lath-like types is high. Because the lath-like type must be perpendicular to the $\langle 001 \rangle$ direction, it is more likely to be found between the $\langle 001 \rangle$ oriented and $\langle 101 \rangle$ oriented grains on the IPF. Table 1 shows the number of cases of each type found according to the grain orientation in the IPF map. The closer to the $\langle 001 \rangle$ oriented grain, the higher the probability of equiaxed and lath-like cellular types grains; the closer to the $\langle 111 \rangle$ oriented grain, the higher the probability of elongated type grains; the closer to the $\langle 101 \rangle$ oriented grain, the higher the probability of finding elongated and lath-like cellular structures grains.

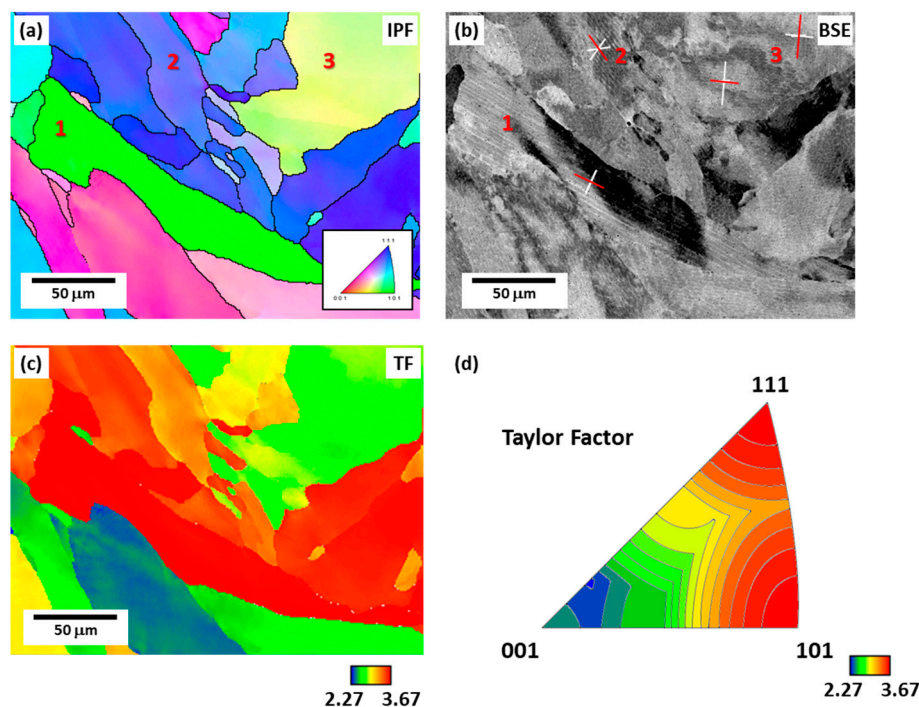


Figure 4. Microstructures of the TD plane: (a) EBSD inverse pole figure (IPF) map, (b) backscattered electron (BSE) image, (c) Taylor factor (TF) map, and (d) TF distribution according to grain orientation. Grain 1, denoted by the number 1, is composed of the lath-like cellular structure; grain 2 consists of both elongated type; and both elongated and lath-like cellular type are observed in grain 3.

Table 1. Type classification according to grain orientation and cell growth direction.

Grain Orientation	Cell Growth Direction	Angle between Grain Orientation and Cell Growth Direction	Cellular Structure Morphology
(111)	[100]	54.7°	Elongated
	[010]	54.7°	Elongated
	[001]	54.7°	Elongated
(110)	[100]	45.0°	Elongated
	[010]	45.0°	Elongated
	[001]	90.0°	Lath-like
(100)	[100]	0°	Equiaxed
	[010]	90.0°	Lath-like
	[001]	90.0°	Lath-like

Figure 5 shows the room temperature engineering compressive stress-strain curves obtained from quasi-static compression tests in two directions, BD and TD, and the average and standard deviation values of yield strength in the two directions are presented in Table 2. The average yield strengths of BD and TD are 520 MPa and 542 MPa and standard deviation of BD and TD are 2.5 MPa and 6.2 MPa, respectively. In other words, the yield strength of TD direction is 22 MPa higher than in the BD direction.

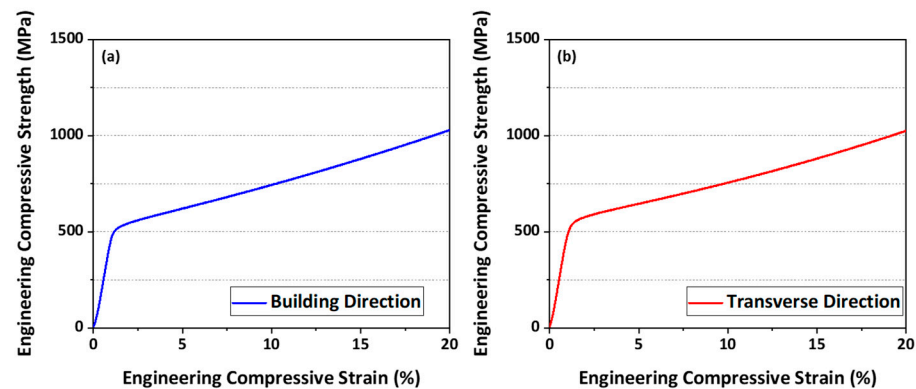


Figure 5. Room temperature engineering stress-strain curves obtained from the quasi-static compression tests in (a) building direction and (b) transverse direction.

Table 2. Quasi-static compression test results of each direction.

Direction	Yield Strength (MPa)	
	Average (MPa)	Standard Deviation
BD	520	2.5
TD	542	6.2

The Taylor factor, which was calculated by considering grain orientation, was analyzed from the EBSD data to explain the yield strength of the additively manufactured SUS316L specimen in relation to the microstructure, particularly the cellular structure morphology. The Taylor factor is a parameter defined according to the relationship among the direction of mechanical property evaluation, slip plane, and slip direction, and is closely related to the yield strength [20]. The yield strength is generally expressed by the Hall–Petch equation as follows [21]:

$$\sigma = \sigma_0 + M\alpha Gb^{1/2}, \quad (1)$$

where σ and σ_0 are the applied stress and friction stress; M is the Taylor factor; α is a constant between zero and unity; G is the shear modulus; b and ρ are Burgers vector and dislocation density. Consequently, the yield strength is observed to be proportional to the Taylor factor.

Figure 4c depicts a map showing the resulting Taylor factor distribution when deformation is applied along the BD in the same regions in Figure 4a,b. The slip plane and slip direction were set to $(111)\langle 110 \rangle$, which is the main slip system of FCC materials. Figure 4d shows the TF distribution map, which shows the correlation between Figure 4a,c, calculated through EBSD when deformed in the BD direction. In Figure 4d, the $\langle 111 \rangle$ oriented grain and $\langle 011 \rangle$ oriented grain have a high Taylor factor, whereas the $\langle 001 \rangle$ oriented grain have a relatively low Taylor factor [22]. Thus, the close relationship between the grain orientation and Taylor factor is highlighted.

Figure 6a shows the IPF map of the BD plane, and Figure 6b,c shows the Taylor factor map when deformation is applied along the BD and TD, respectively, along with the Taylor factor values. When evaluating the mechanical properties in the BD and TD, the Taylor factor values were calculated to be 2.972 and 3.119, respectively, and there was a higher Taylor factor value along the TD. As can be seen from Equation (1), this is consistent with the compression test result, in which the yield strength in the TD is higher. Figure 6d shows the distribution of the grain orientation parallel to the BD and TD. The $BD//\langle 001 \rangle$, $TD//\langle 111 \rangle$, and $TD//\langle 101 \rangle$ textures are predominant. From Figure 4d, it can also be seen that the Taylor factor is related to the grain orientation. In the BD, the $\langle 001 \rangle$ texture with a low Taylor factor is dominant; thus, the average Taylor factor value is low. In contrast, in the TD, the average Taylor factor value is high because of the $\langle 101 \rangle$ and $\langle 111 \rangle$ textures. In summary, the $TD//\langle 101 \rangle$ and $TD//\langle 111 \rangle$ textures are developed along

the TD, resulting in a high Taylor factor and consequently, a higher yield strength than that along the BD.

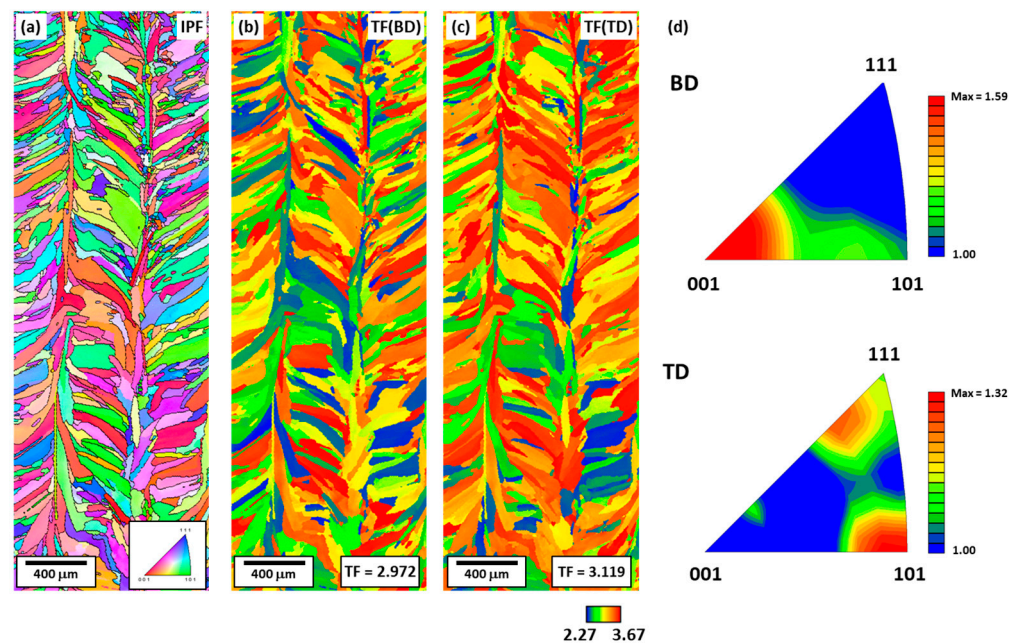


Figure 6. Microstructures of the BD plane: (a) EBSD IPF map; TF map under deformation parallel to (b) BD and (c) TD; and (d) IPFs along BD and TD showing orientation distribution.

Hardness is also related to the Taylor factor, and the higher the Taylor factor value, the higher the hardness [23–25]. Table 3 presents the hardness values according to the type defined by the cellular structure morphology. The hardness of equiaxed, elongated, and lath-like cellular structures were 218 HV, 244 HV, and 226 HV, respectively, and the standard deviations were 6.6 HV, 7.3 HV, and 14.5 HV, respectively. Therefore, the hardness was the highest in the elongated cellular structure and the lowest in the equiaxed cellular structure. In addition, the standard deviation was the highest in the lath-like cellular structure. The elongated cellular structure is more easily observed when approaching the $\langle 111 \rangle$ oriented grain, and additionally, the closer it gets to the $\langle 111 \rangle$ oriented grain, the higher the Taylor factor value; thus, the hardness value is also increased. Conversely, because equiaxed type is mainly found close to the $\langle 001 \rangle$ oriented grain, its Taylor factor value and hardness are relatively low. In the case of lath-like type, which is observed between the $\langle 001 \rangle$ and $\langle 101 \rangle$ oriented grains, there is a higher probability of it being observed in the $\langle 001 \rangle$ oriented grain; therefore, it has a low hardness with a large standard deviation of hardness.

Table 3. Vickers hardness according to cellular structure morphology.

Specimen	Cellular Structure Morphology	Average	Standard Deviation
SUS316L	Equiaxed	218 HV	6.6
	Elongated	244 HV	7.3
	Lath-like	226 HV	14.5

The area fraction of each cellular structure morphology was measured from 50 SEM micrographs of the TD and BD plane using an image analyzer, respectively (Figure 7). In the TD planes, the fraction increases in the order of lath-like (18%), elongated (35%), and equiaxed (47%) whereas in the BD planes, the fraction increases in order of lath-like (24%), elongated (25%) and equiaxed (51%). In both planes, the cellular structure area fraction tends to be similar, but the area fraction values are different. TD plane has high area fraction of elongated type with a high Taylor factor and hardness, whereas BD plane has high area

fraction of equiaxed type with a low Taylor factor and hardness. This is consistent with the tendency that the yield strength in the TD direction is higher than that in the BD direction.

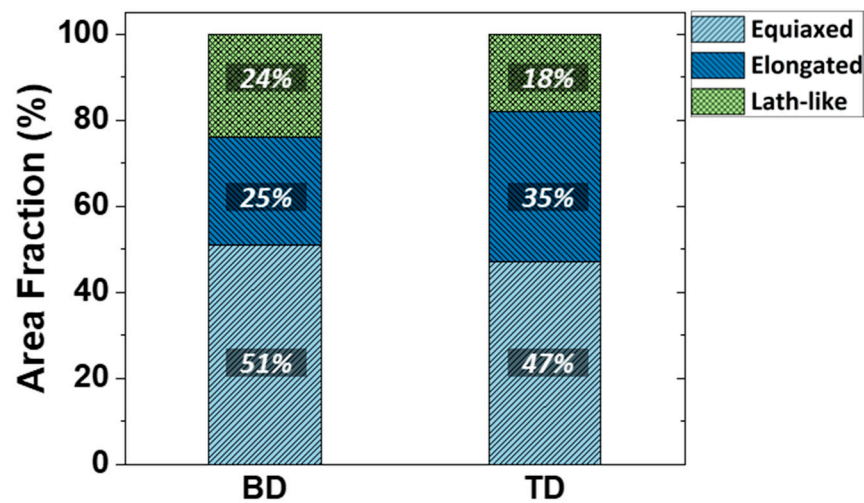


Figure 7. Area fraction of each cellular structure morphology in BD and TD planes.

In conclusion, because epitaxial growth with the directionality of the cellular structure occurs in the additively manufactured specimen, the cellular structure morphology varies depending on the angle between the observation and cell growth directions. Therefore, the cellular structure morphology is determined, which can have a high probability of appearance in grains with a specific grain orientation, and because the grain orientation can affect the Taylor factor, the morphology of the cellular structure affects the mechanical properties of the specimen, such as yield strength and hardness. In other words, in this study, it is confirmed that the elongated cellular structure morphology has a high probability of being found in grains with high Taylor factor, so the elongated cellular structure morphology has a higher hardness compared to other morphologies. As a result, the yield strength of the TD direction is higher because the TD plane has a higher elongated cellular structure fraction than the BD direction. Thus, yield strength of austenitic stainless steel additively manufactured can be predicted through cellular structure morphology and it can be helpful in designing 3D printed structures.

4. Conclusions

In this study, the yield strength of austenitic stainless steel additively manufactured using the DED method was explained in relation to the morphology and orientation of its cellular structure. The cellular structure appearing during AM underwent epitaxial growth along the $\langle 100 \rangle$ direction, resulting in equiaxed, elongated, and lath-like types, depending on the observation direction. In the specimen, the BD// $\langle 001 \rangle$ texture, in which the lath-like type was mainly observed along the BD, and the TD// $\langle 111 \rangle$ and $\langle TD \rangle$ // $\langle 101 \rangle$ textures, where the elongated type was mainly observed along the TD, were found. The values of the Taylor factor affecting the mechanical properties differed depending on the orientation. The equiaxed type had a low Taylor factor value; the elongated type had a high Taylor factor value; and the lath-like type had low or high Taylor factor values depending on the observation direction. Therefore, in the TD, the yield strength was higher than that in the BD owing to the microstructure having a high Taylor factor. From these research results, the possibility of application to predicting yield from the fraction or cellular structure morphology was confirmed.

Author Contributions: D.W.K. performed an analysis on the correlation between grain orientation and cellular structure morphology. S.B.H. conducted the experiment and discussed the results related to mechanical properties. Y.S.L., D.Y.P. and H.-J.L. fabricated additively manufactured specimens and discussed additive manufacturing. S.H.P. discussed the microstructure analysis and correlation between microstructure and yield strength. H.S. designed and performed all the experiments. D.W.K. and H.S. wrote the manuscript with contributions from the other authors. All authors commented on the final manuscript and conclusions of this study. All authors have read and agreed to the published version of the manuscript.

Funding: This study has been conducted with the support of the Korea Institute of Industrial Technology as “AI platforms for vision systems and applications (kitech JA-23070)”.

Institutional Review Board Statement: Not applicable.

Informed Consent Statement: Not applicable.

Data Availability Statement: The data presented in this study are available upon request from the corresponding author. The data are not publicly available due to confidentiality.

Acknowledgments: This study was supported by the Korea Institute of Industrial Technology as “AI platforms for vision systems and applications (kitech JA-23070)”.

Conflicts of Interest: The authors declare no conflict of interest.

References

1. Barkia, B.; Aubry, P.; Haghi-Ashtiani, P.; Auger, T.; Gosmain, L.; Schuster, F.; Maskrot, H. On the origin of the high tensile strength and ductility of additively manufactured 316 L stainless steel: Multiscale investigation. *J. Mater. Sci. Technol.* **2020**, *41*, 209–218. [[CrossRef](#)]
2. Kong, D.; Dong, C.; Wei, S.; Ni, X.; Zhang, L.; Li, R.; Wang, L.; Man, C.; Li, X. About metastable cellular structure in additively manufactured austenitic stainless steels. *Addit. Manuf.* **2021**, *28*, 101804. [[CrossRef](#)]
3. Melzer, D.; Dzugan, J.; Koukolikova, M.; Rzepa, S.; Vavrik, J. Structural integrity and mechanical properties of the functionally graded material based on 316 L/IN718 processed by DED technology. *Mater. Sci. Eng. A* **2021**, *811*, 141038. [[CrossRef](#)]
4. Oh, W.J.; Lee, W.J.; Kim, M.S.; Jeon, J.B.; Shim, D.S. Repairing additive-manufactured 316 L stainless steel using direct energy deposition. *Opt. Laser. Technol.* **2019**, *117*, 6–17. [[CrossRef](#)]
5. Yadollahi, A.; Shamsaei, N. Additive manufacturing of fatigue resistant materials: Challenges and opportunities. *Int. J. Fatigue* **2017**, *98*, 14–31. [[CrossRef](#)]
6. Li, C.; Liu, Z.Y.; Fang, X.Y.; Guo, Y.B. Residual stress in metal additive manufacturing. *Procedia CIRP* **2018**, *71*, 348–353. [[CrossRef](#)]
7. Haley, J.C.; Schoenung, J.M.; Lavernia, E.J. Modeling particle impact on the melt pool and wettability effects in laser directed energy deposition additive manufacturing. *Mater. Sci. Eng. A* **2019**, *761*, 138052. [[CrossRef](#)]
8. Beese, A.; Carroll, B.E. Review of mechanical properties of Ti-6Al-4V made by laser-based additive manufacturing using powder feedstock. *J. Miner. Met. Mater. Soc.* **2016**, *68*, 3. [[CrossRef](#)]
9. Liu, L.; Ding, Q.; Zhong, Y.; Zou, J.; Wu, J.; Chiu, Y.L.; Li, J.; Zhang, Z.; Yu, Q.; Shen, Z. Dislocation network in additive manufactured steel breaks strength-ductility trade-off. *Mater. Today* **2018**, *21*, 354–361. [[CrossRef](#)]
10. Wang, Y.M.; Voisin, T.; McKeown, J.T.; Ye, J.; Caltà, N.P.; Li, Z.; Zeng, Z.; Zhang, Y.; Chen, W.; Roechling, T.T.; et al. Additively manufactured hierarchical stainless steels with high strength and ductility. *Nat. Mater.* **2018**, *17*, 63–71. [[CrossRef](#)]
11. Kim, D.K.; Woo, W.; Kim, E.Y.; Choi, S.H. Microstructure and mechanical characteristics of multi-layered materials composed of 316 L stainless steel and ferritic steel produced by direct energy deposition. *J. Alloys Compd.* **2019**, *774*, 896–907. [[CrossRef](#)]
12. Saboori, A.; Aversa, A.; Marchese, G.; Biamino, S.; Lombardi, M.; Fino, P. Application of directed energy deposition-based additive manufacturing in repair. *Appl. Sci.* **2019**, *9*, 3316. [[CrossRef](#)]
13. Cederberg, E.; Hosseini, V.A.; Kumara, C.; Karlsson, L. Physical simulation of additively manufactured super duplex stainless steels—Microstructure and properties. *Addit. Manuf.* **2020**, *34*, 101269. [[CrossRef](#)]
14. Xia, Z.; Shi, J.; Shi, T.; Sun, C.; Qiu, D. Microstructure evolution and mechanical properties of reduced activation steel manufactured through laser directed energy deposition. *Addit. Manuf.* **2020**, *33*, 101114. [[CrossRef](#)]
15. Kok, Y.; Tan, X.P.; Nai, M.L.S.; Loh, N.H.; Liu, E.; Tor, S.B. Anisotropy and heterogeneity of microstructure and mechanical properties in metal additive manufacturing: A critical review. *Mater. Des.* **2018**, *139*, 565–586. [[CrossRef](#)]
16. Li, Z.; He, B.; Guo, Q. Strengthening and hardening mechanisms of additively manufactured stainless steels: The role of cell sizes. *Scr. Mater.* **2020**, *177*, 17–21. [[CrossRef](#)]
17. Ronneberg, T.; Davies, C.M.; Hooper, P.A. Revealing relationships between porosity, microstructure and mechanical properties of laser powder bed fusion 316 L stainless steel through heat treatment. *Mater. Des.* **2020**, *189*, 108481. [[CrossRef](#)]
18. Kong, D.; Ni, X.; Dong, C.; Zhang, L.; Man, C.; Yao, J.; Xiao, K.; Li, X. Heat treatment effect on the microstructure and corrosion behavior of 316 L stainless steel fabricated by selective laser melting for proton exchange membrane fuel cells. *Electrochim. Acta* **2018**, *20*, 293–303. [[CrossRef](#)]

19. Karthik, G.M.; Kim, H.S. Heterogeneous aspects of additive manufactured metallic parts: A review. *Met. Mater. Int.* **2021**, *27*, 1–39. [[CrossRef](#)]
20. Shen, J.; Li, Y.L.; Wei, Q. Statistics deviation of Taylor factors for polycrystalline metals with application to pure magnesium. *Mater. Sci. Eng. A* **2013**, *582*, 270–275. [[CrossRef](#)]
21. Gubicza, J.; Chinh, N.Q.; Csanadi, T.; Langdon, T.G.; Ungar, T. Microstructure and strength of severely deformed fcc metals. *Mater. Sci. Eng. A* **2007**, *462*, 86–90. [[CrossRef](#)]
22. Harte, A.; Atkinson, M.; Preuss, M.; Quinta da Fonseca, J. A statistical study of the relationship between plastic strain and lattice misorientation on the surface of a deformed Ni-based superalloy. *Acta Mater.* **2020**, *195*, 555–570. [[CrossRef](#)]
23. Zhao, M.; Ji, X.; Li, B.; Laing, S.Y. Effect of crystallographic orientation on the hardness of polycrystalline materials. *J. Mech. Eng. Sci.* **2019**, *233*, 3182–3192. [[CrossRef](#)]
24. Zhao, M.; Ji, X.; Liang, S.Y. Force prediction in micro-grinding maraging steel 3J33b considering the crystallographic orientation and phase transformation. *Int. J. Adv. Manuf. Technol.* **2019**, *103*, 2821–2836. [[CrossRef](#)]
25. Miura, T.; Fujii, K.; Fukuya, K.; Takashima, K. Influence of crystal orientation on hardness and nanoindentation deformation in ion-irradiated stainless steels. *J. Nucl. Mater.* **2011**, *417*, 984–987. [[CrossRef](#)]

Disclaimer/Publisher’s Note: The statements, opinions and data contained in all publications are solely those of the individual author(s) and contributor(s) and not of MDPI and/or the editor(s). MDPI and/or the editor(s) disclaim responsibility for any injury to people or property resulting from any ideas, methods, instructions or products referred to in the content.